nature chemistry

ARTICLES

PUBLISHED ONLINE: 24 APRIL 2017 | DOI: 10.1038/NCHEM.2764

π-electron $S = ½$ quantum spin-liquid state in an ionic polyaromatic hydrocarbon

Yasuhiro Takabayashi[1], Melita Menelaou[1,2], Hiroyuki Tamura[1], Nayuta Takemori[3], Takashi Koretsune[3], Aleš Štefančič[1,4], Gyöngyi Klupp[4], A. Johan C. Buurma[4], Yusuke Nomura[5], Ryotaro Arita[2,3], Denis Arčon[6,7], Matthew J. Rosseinsky[8]* and Kosmas Prassides[1,2]*

Molecular solids with cooperative electronic properties based purely on π electrons from carbon atoms offer a fertile ground in the search for exotic states of matter, including unconventional superconductivity and quantum magnetism. The field was ignited by reports of high-temperature superconductivity in materials obtained by the reaction of alkali metals with polyaromatic hydrocarbons, such as phenanthrene and picene, but the composition and structure of any compound in this family remained unknown. Here we isolate the binary caesium salts of phenanthrene, $Cs(C_{14}H_{10})$ and $Cs_2(C_{14}H_{10})$, to show that they are multiorbital strongly correlated Mott insulators. Whereas $Cs_2(C_{14}H_{10})$ is diamagnetic because of orbital polarization, $Cs(C_{14}H_{10})$ is a Heisenberg antiferromagnet with a gapped spin-liquid state that emerges from the coupled highly frustrated Δ-chain magnetic topology of the alternating-exchange spiral tubes of $S = ½$ $(C_{14}H_{10})^{\bullet-}$ radical anions. The absence of long-range magnetic order down to 1.8 K ($T/J \approx 0.02$; J is the dominant exchange constant) renders the compound an excellent candidate for a spin-½ quantum-spin liquid (QSL) that arises purely from carbon π electrons.

Conventional Heisenberg antiferromagnets (AFMs) typically exhibit magnetic long-range order (LRO) below the Néel temperature, T_N. However, this emergence of static order can be suppressed in the presence of geometrical frustration[1]—the arrangement of coupled magnetic units on lattices that comprise triangular or tetrahedral building blocks leads to a situation in which it is impossible to satisfy simultaneously all near-neighbour exchange interactions. This results in a spin-liquid state with a highly degenerate ground state in which strong magnetic fluctuations persist down to low temperatures. The fluctuations are further enhanced in the quantum limit of $S = ½$ spins and the resulting QSL prevails over AFM–LRO even at zero temperature[2,3]. To date, the candidates for experimental realization of QSLs remain very few. Prominent among these are the Cu^{2+} inorganic minerals herbertsmithite ($ZnCu_3(OH)_6Cl_2$) (ref. 4) and vesignieite ($BaCu_3V_2O_8(OH)_2$) (ref. 5) with Cu^{2+} $S = ½$ ions arranged on two-dimensional (2D) Kagomé networks of corner-sharing triangular units, and the organic compounds κ-(BEDT-TTF)$_2$Cu$_2$(CN)$_3$ (BEDT-TTF, bis(ethylenedithio)tetrathiafulvalene), EtMe$_3$Sb[Pd(dmit)$_2$]$_2$ (dmit, 1,3-dithiole-2-thione-4,5-dithiolate) and κ-H$_3$(Cat-EDT-TTF)$_2$ (Cat, catechol) with a direct 2D edge-sharing triangular lattice topology[6–8].

In our search for novel conducting and magnetic functionalities, we have been exploring the electronic properties of materials in which the active components of the extended structures are π-electron open-shell molecular units. These systems crystallize in architectures of varied dimensionality that range from 1D to 3D and encompass molecular metals and superconductors, such as organic charge-transfer salts[9] and the alkali fullerides[10–12], which provide the highest T_c (38 K) (ref. 13) together with molecular magnets[14], including QSLs[6–8] and quantum-spin chains and ladders[15–17]. In particular, the interest in all-carbon π-electron systems was recently revived by the report that alkali intercalation of a polyaromatic hydrocarbon (PAH), the five-membered-ring picene $C_{22}H_{14}$, led to a superconductor with $T_c = 18$ K, but of unknown composition and structure[18]. Superconductivity was subsequently reported in alkali-intercalated PAHs with three (phenanthrene, $C_{14}H_{10}$) and seven (1,2:8,9-dibenzopentacene, $C_{30}H_{18}$) aromatic rings ($T_c = 5$ and 33 K, respectively)[19,20]. However, despite the flare of experimental and theoretical activity[21–26], the results have not been reproduced and the identity of any compound in this family has remained unknown, which reflects the unavailability of phase-pure samples because of difficulties in controlling the reactivity of alkali metals at high temperature[18–20].

Here we isolated two members of the family of alkali intercalated PAH solids—namely, the binary salts of phenanthrene with compositions $Cs(C_{14}H_{10})$ (**1**) and $Cs_2(C_{14}H_{10})$ (**2**), which contain the phenanthride radical mono- and dianions, respectively—using a solution-based route under mild conditions that avoids the competing decomposition of PAH molecules under a high-temperature reaction with alkali metals. Analysis of the structural and electronic properties complemented by first-principles calculations established both materials as two-orbital strongly correlated Mott insulators. Dianion salt **2** is a low-spin, $S = 0$ system with an orbitally polarized insulating state, which adiabatically connects to a band-insulating state. However, the $S = ½$ $(C_{14}H_{10})^{\bullet-}$ radical anions in **1** are incorporated into a magnetic network of Heisenberg antiferromagnetically coupled spiral magnetic tubes. Coupling between neighbouring tubes via corner-sharing triangular units leads to a complex highly frustrated 3D spin topology of unequal-leg spin chains that run along the crystallographic c axis and corner-sharing Δ chains[27] that run along the b direction. The magnetic behaviour of the

[1]World Premier International–Advanced Institute for Materials Research (WPI-AIMR), Tohoku University, Sendai 980-8577, Japan. [2]Japan Science and Technology Agency, ERATO Isobe Degenerate π-Integration Project, Tohoku University, Sendai 980-8577, Japan. [3]RIKEN Center for Emergent Matter Science (CEMS), 2-1, Hirosawa, Wako, Saitama 351-0198, Japan. [4]Department of Chemistry, Durham University, Durham DH1 3LE, UK. [5]Department of Applied Physics, University of Tokyo, Tokyo 113-8656, Japan. [6]Jozef Stefan Institute, Jamova cesta 39, SI-1000 Ljubljana, Slovenia. [7]Faculty of Mathematics and Physics, University of Ljubljana, Jadranska cesta 19, 1000 Ljubljana, Slovenia. [8]Department of Chemistry, University of Liverpool, Liverpool L69 7ZD, UK. *e-mail: k.prassides@wpi-aimr.tohoku.ac.jp; m.j.rosseinsky@liverpool.ac.uk

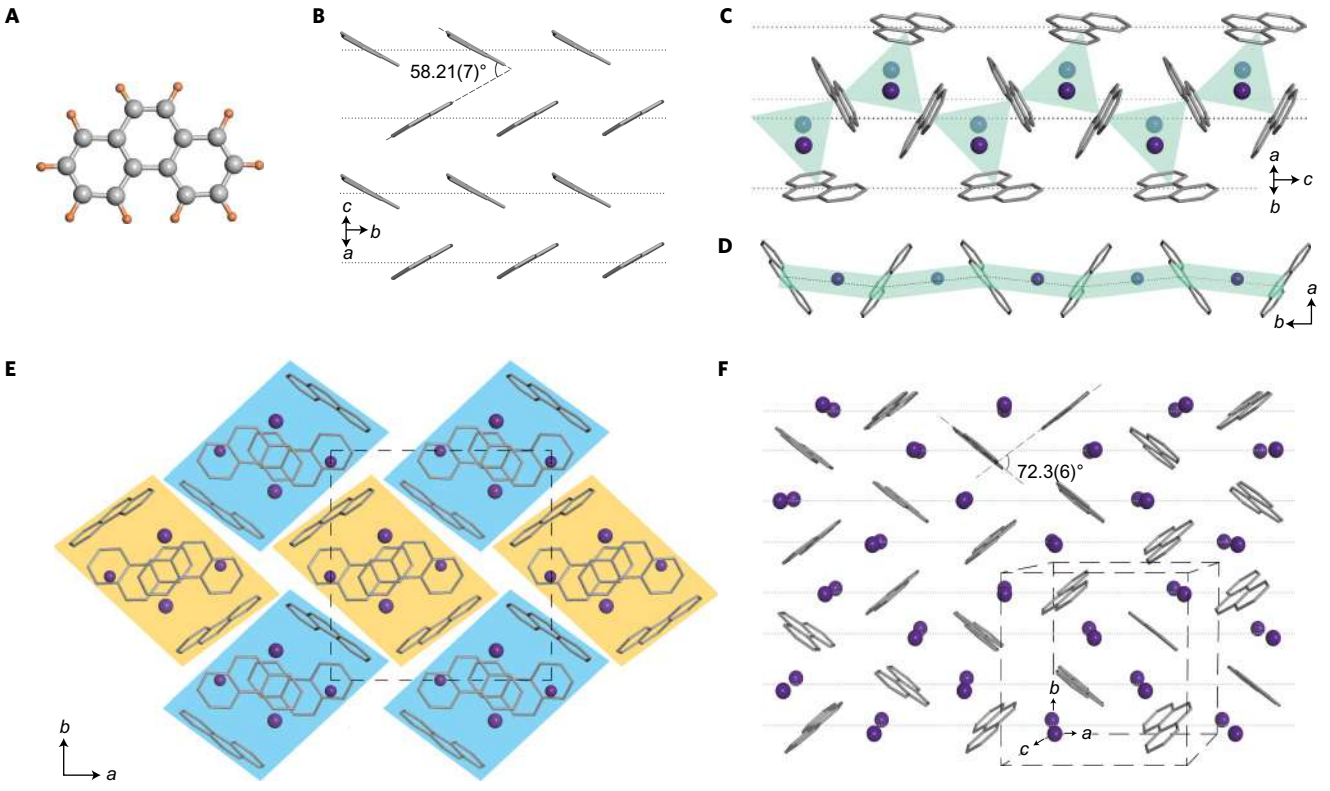

Figure 1 | Crystal structures of pristine phenanthrene and its caesium and dicaesium salts. A, The phenanthrene molecule, $C_{14}H_{10}$. **B**, The herringbone structure of pristine phenanthrene (space group $P2_1$, lattice constants: $a = 8.472(4)$ Å; $b = 6.166(4)$ Å; $c = 9.467(5)$ Å; $\beta = 98.01(5)°$; and $V = 489.7(5)$ Å^3 at 297 K) (ref. 28). The dotted lines mark the slip-stacked 1D molecular columns along the *b* axis; the interplanar angles between the mean plane of each molecule and that of its neighbours are 58.21(7)°. **C**, The crystal structure of orthorhombic $Cs(C_{14}H_{10})$ is built by tubular assemblies of vertex-sharing triangularly arranged trimers of $(C_{14}H_{10})^{\bullet-}$ radical anions (centre-to-centre connections are depicted in green shading) that align along the *c* axis. The dotted lines through the centres of the molecules define the spiral molecular tubes. The herringbone-packing motif of the pristine phenanthrene solid has been abandoned and Cs^+ incorporation is accompanied by a ~16% volume expansion. **D**, Zigzag chains of $(C_{14}H_{10})^{\bullet-}$ ions from neighbouring tubes running along the *b* axis. **E**, The basal plane projection of the structure of $Cs(C_{14}H_{10})$ emphasizes the parallel stacking of the individual quasi-1D molecular tubes perpendicular to the *ab* plane. Each tube (shown in gold or blue shading) is surrounded by four neighbours oriented at nearly right angles (at 87.670(8)° (blue shading) or at 92.330(8)° (gold shading)). The unit cell is depicted by dashed lines. **F**, Perspective view down the *c* axis of the crystal structure of monoclinic $Cs_2(C_{14}H_{10})$. The unit cell is depicted by dashed lines. Herringbone packing is also abandoned and Cs^+ incorporation is accompanied by a ~27% volume expansion. Dotted lines go through the centres of molecules with parallel ring orientation. The interplanar angles are 72.3(6)°. C, grey; Cs, purple; H, orange.

material, which shows no magnetic order down to 1.8 K, is compatible with that of a gapped QSL.

Results and discussion

Synthesis and crystal structures. Pristine phenanthrene adopts a monoclinic structure[28] in which the planar molecules (Fig. 1A) form a herringbone-packing assembly of slip-stacked 1D columns along the short *b* axis of the unit cell with interplanar angles between neighbouring molecules in adjacent chains of 58.21(7)° (Fig. 1B). Reaction of 1 equiv. caesium and 1 equiv. phenanthrene in rigorously dried THF under mild heating affords a dark olive-green crystalline material of composition $Cs(C_{14}H_{10})$. Similarly, the solvent-free dicaesium phenanthride $Cs_2(C_{14}H_{10})$ is isolated from solution as a black crystalline powder by reacting 2 equiv. caesium with 1 equiv. phenanthrene in dry THF under mild heating. Powder diffraction shows that both materials are of excellent crystallinity (Fig. 2a,b), in sharp contrast to those obtained by solid-state routes[18–20].

The high quality of the diffraction data permitted a straightforward determination of the crystal structures of both compounds. Space-group assignment and the extraction of unit-cell dimensions were performed by the LeBail pattern-decomposition technique. This was followed by an initial structural model generation for each system using phenanthrene units modelled as rigid bodies without internal degrees of freedom and Cs^+ ions. Structural model optimization was then performed with a direct-space simulated-annealing global-optimization technique. Finally, refinement of the structures was undertaken by a Rietveld analysis of the diffraction data with an excellent agreement between observed and calculated profiles achieved for both systems (Fig. 2a,b). $Cs(C_{14}H_{10})$ crystallizes in the non-centrosymmetric primitive orthorhombic $P2_12_12_1$ space group with two crystallographically distinct Cs^+ ions and two phenanthrene units in a unit cell of dimensions $a = 14.4388(2)$ Å, $b = 15.0250(2)$ Å and $c = 10.0842(1)$ Å at 30 K (agreement factors: weighted-profile *R*-factor, $R_{wp} = 4.80\%$ and expected *R*-factor, $R_{exp} = 2.41\%$). $Cs_2(C_{14}H_{10})$ is monoclinic (space group $P2_1/a$) with one crystallographically distinct phenanthrene unit and two Cs^+ ions per unit cell (lattice constants at ambient temperature: $a = 11.8129(2)$ Å, $b = 11.4667(2)$ Å, $c = 9.8269(1)$ Å, $\beta = 110.894°(1)$; agreement factors: $R_{wp} = 1.95\%$, $R_{exp} = 1.98\%$). The fitted parameters and selected bond distances are summarized in Supplementary Tables 1–4.

The crystal-structure analysis of both samples reveals that alkali intercalation and phenanthrene reduction are accompanied by drastic structural changes as the herringbone-packing motif of the pristine material is abandoned. Instead, the structure of **1**, which expands by ~40 Å^3 per phenanthrene on intercalation, is built by

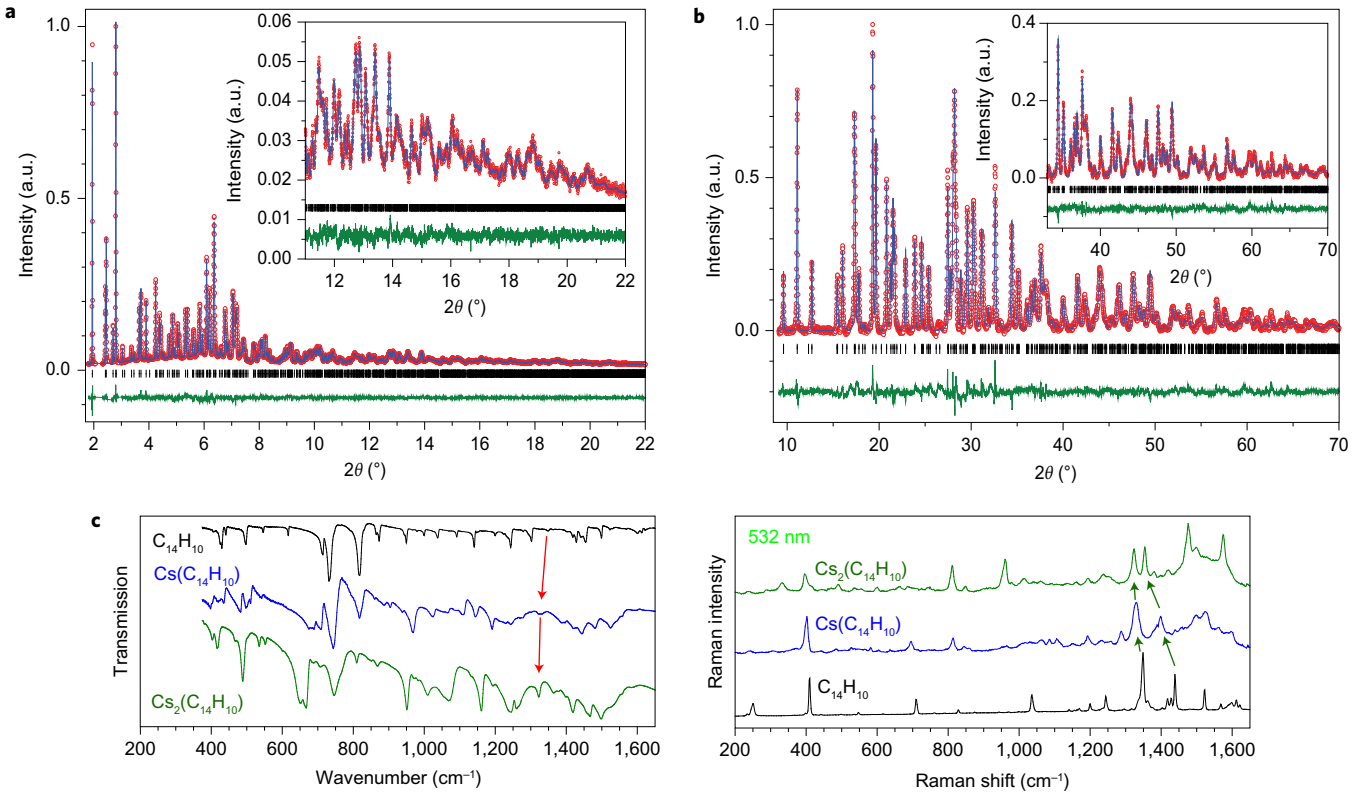

Figure 2 | Structural and vibrational characterization of caesium phenanthride salts. a, Final observed (red circles) and calculated (blue solid line) synchrotron X-ray ($\lambda = 0.35420$ Å) powder diffraction profiles for the $Cs(C_{14}H_{10})$ (**1**) sample at 30 K. **b**, Final observed (red circles) and calculated (blue solid line) X-ray ($\lambda = 1.54056$ Å, Cu $K_{\alpha 1}$) powder diffraction profiles (after background subtraction) for the $Cs_2(C_{14}H_{10})$ (**2**) sample at ambient temperature. The lower green solid lines in both **a** and **b** show the difference profiles and the tick marks show the reflection positions. The insets in both **a** and **b** show expanded views of the corresponding diffraction profiles at high Bragg angles. **c**, Infrared (left) and Raman ($\lambda = 532$ nm excitation, right) spectra of $C_{14}H_{10}$ (black), $Cs(C_{14}H_{10})$ (blue) and $Cs_2(C_{14}H_{10})$ (green) at ambient temperature. Green arrows mark the shifts of two characteristic Raman peaks. The 1,349 cm^{-1} peak redshifts by 17 and 7 cm^{-1} on uptake of one and two electrons, respectively; the infrared spectrum shows an identical shift (red arrows). The 1,439 cm^{-1} peak shows a linear redshift of ~42 cm^{-1} per elementary charge.

triangularly arranged trimeric units of $(C_{14}H_{10})^{\bullet -}$ ions (Fig. 1C). The repeat units share vertices to form spiral tubes that align along the *c* axis. The tubes (of size 11.9 $Å^2$) adopt a bipartite packing motif in which each is surrounded by four neighbours positioned approximately at right angles (Fig. 1E). This results in the formation of zigzag chains that run parallel to the *b* axis and comprise $(C_{14}H_{10})^{\bullet -}$ ions from neighbouring tubes (Fig. 1D). The Cs^+ cations are incorporated inside the tubes and coordinate to benzene rings of adjacent phenanthride ions with $Cs^+ \cdots C$ separations in the range of 3.119(3)–3.736(2) Å at 30 K (Supplementary Table 2), which implies a rather strong binding of the metal ions to the phenanthrene surface. Further changes in molecular packing occur on intercalation of the second Cs^+ per formula unit to afford **2**. Every other phenanthrene unit flips along the stacking direction of the pristine material in such a way as to present its benzene rings for optimal coordination by Cs^+ ions that occupy interstitial sites above and below the molecular plane (Fig. 1F). The Cs^+ ions also bind to benzene rings of non-flipped adjacent $(C_{14}H_{10})^{2-}$ units. The $Cs^+ \cdots C$ separations vary between 3.148(7) and 3.72(1) Å at room temperature (Supplementary Table 4), again indicative of strong Cs^+–π interactions. The resulting expanded structure (by ~66 $Å^3$ per phenanthrene) is that of an assembly of zigzag chains of $(C_{14}H_{10})^{2-}$ units alternately tilted by 72.3(6)°. The Raman and infrared spectra of **1** and **2** show a softening and broadening of the vibrational modes on reduction, consistent with the antibonding nature of the lowest unoccupied molecular orbital (LUMO) and the theoretically predicted[29] strong electron–phonon coupling, respectively (Fig. 2c and Supplementary Fig. 1). Although softening is mostly monotonic, it is rarely linear with increasing charge (Supplementary Table 5), unlike that for C_{60} in which the $A_g(2)$ mode downshifts quasilinearly (~6 cm^{-1} per charge)[30,31].

Electronic states—insulating behaviour and absence of magnetic order. Magnetization data from both compounds (Fig. 3) do not show evidence for either metallic behaviour or superconductivity. The molar magnetic susceptibility, $\chi(T)$ of **1** displays a broad maximum at ~40 K together with a sharp upturn at low *T* caused by impurity-spin contributions. There is no deviation between zero-field-cooled (ZFC) and field-cooled (FC) measurements. Above 100 K, $\chi(T)$ follows the Curie–Weiss law to yield an effective moment, $\mu_{eff} = 1.76(1)\ \mu_B$ per phenanthride (consistent with $S = ½$ per phenanthride) and a Weiss temperature, $\Theta = -72.5(1)$ K, indicative of strong AFM exchange interactions. $\chi(T)$ of **2** is drastically different and consistent with the presence of a low-spin diamagnetic $(C_{14}H_{10})^{2-}$ anion.

A more definitive characterization of the magnetic properties is achieved by electron paramagnetic resonance (EPR) spectroscopy, which directly measures spin susceptibilities of individual components. At ambient temperature, the X-band EPR spectrum of **1** comprises two components (Fig. 4a): a majority nearly ideal Lorentzian line at $g = 2.0007(3)$ with width $\Delta B = 15.29(1)$ mT and a barely discernible minority *g*-factor-broadened line. The proximity of *g* to the free-electron value, $g_e = 2.0023$, signifies the presence of electronically active $(C_{14}H_{10})^{\bullet -}$ radical anions and a nearly complete electron transfer from Cs to $C_{14}H_{10}$. Neither component shows Dysonian lineshape asymmetry, characteristic of a metallic state. We

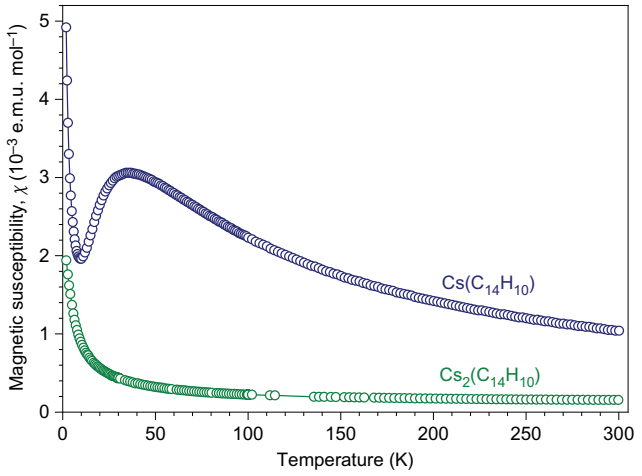

Figure 3 | Evolution of magnetic properties on the reduction of phenanthrene. Temperature dependence of the molar magnetic susceptibility, χ, of **1** (blue circles) and **2** (green circles) measured in FC runs at 1 and 5 T, respectively. $\chi(T)$ of **2** follows the Curie–Weiss law and yields: a temperature-independent term, $\chi_0 = 1.21(9) \times 10^{-4}$ e.m.u. mol^{-1}; a Curie constant, $C = 0.01065(5)$ e.m.u. K mol^{-1} (which corresponds to a spin concentration of 0.03 spins per molecule, ascribed to lattice defects); and a Weiss temperature, $\Theta = -3.78(3)$ K.

conclude that **1** is an insulator. The intensity of the minority component (~5% of all spins) follows a Curie-like temperature dependence (Fig. 4b) and is ascribed to impurity or defect states. A similar low-intensity Curie-like line characterizes the EPR spectrum of diamagnetic **2**, which is thus also insulating (Supplementary Fig. 2). The non-Fano lineshape of the infrared peaks (Fig. 2c) is consistent with the insulating state assignment of **1** and **2**. On the other hand, the intensity of the main broad component in the EPR spectrum of **1** mimics the temperature response of the SQUID (superconducting quantum interference device) magnetic susceptibility. It first increases on cooling, reaches a broad maximum at ~42 K and then starts to decrease approaching zero as $T \rightarrow 0$ K (Fig. 4b), and thereby implies the presence of some spin gap in the excitation spectrum. The low-temperature suppression of the main EPR line is not accompanied by the emergence of an antiferromagnetic resonance characteristic of a transition to an AFM–LRO state.

The magnetic data of **1**—a broad $\chi(T)$ maximum at T_{max} and the emergence of a spin gap at lower temperatures—are reminiscent of the response of $S = ½$ antiferromagnetic alternating-exchange Heisenberg spin chains[32]. Indeed, good agreement with the combined EPR and SQUID spin-susceptibility data over the entire temperature range is found for this model—the global fit (Fig. 4b) yields an intrachain exchange constant, $J/k_B = 77.9(3)$ K, an alternation parameter, $\alpha = 0.687(5)$, and a Curie constant, $C = 0.301(1)$ e.m.u. K mol^{-1} (consistent with $S = ½$ per phenanthride). However, despite the excellent fit of the purely 1D magnetic model to the experimental data, the existence of interchain magnetic coupling is immediately evident in the temperature evolution of the EPR linewidth, ΔB. The gradual increase in ΔB at low temperatures (Supplementary Fig. 3) cannot be rationalized solely within 1D models[33]. It implies the growth of spin correlations and necessitates a finite interchain magnetic exchange[34]. This, in turn, is known to stabilize AFM–LRO for both disorder-free and disordered systems[35]. Then, the experimentally observed robustness of the quantum

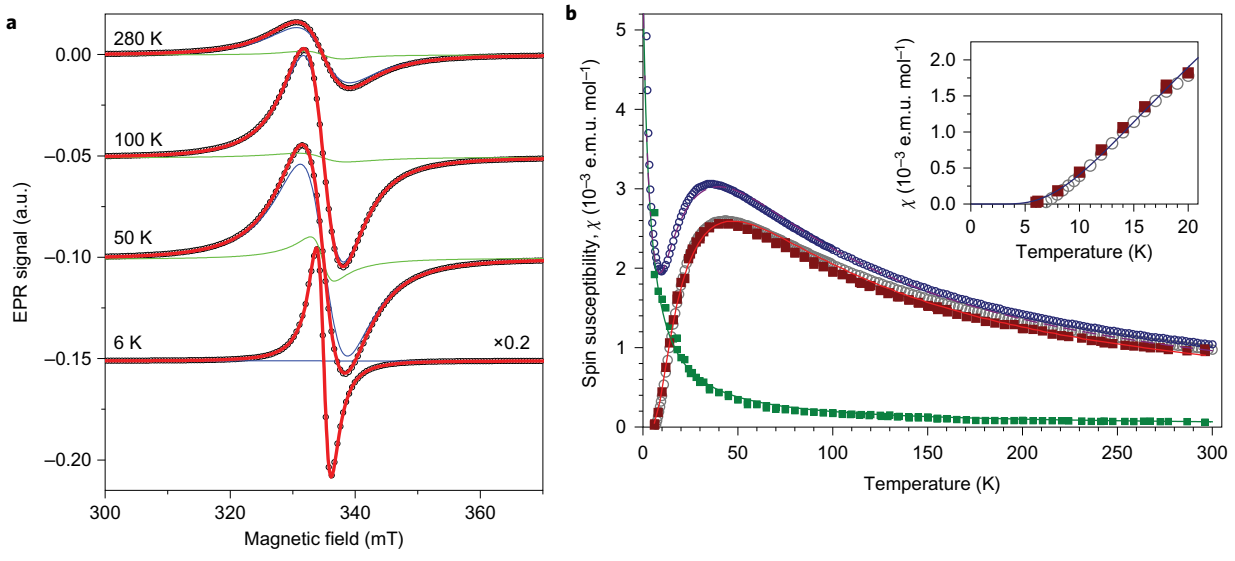

Figure 4 | EPR spectroscopy and spin susceptibility of Cs($C_{14}H_{10}$). a, Temperature evolution of the X-band EPR spectra for Cs($C_{14}H_{10}$) powder (open circles). Solid red lines are fits of the data to a model of two overlapping components: the main broad one with a Lorentzian lineshape (blue line) dominates the spectra above ~15 K, whereas the much narrower minority one ($\Delta B_x = 1.62(2)$ mT, $\Delta B_y = \Delta B_z = 0.47(2)$ mT, green line) has a lineshape characteristic of a small uniaxial g-factor anisotropy ($g_{xx} = 1.998(1)$ and $g_{yy} = g_{zz} = 2.001(1)$) and prevails at the lowest temperatures where it solely accounts for the spectrum at 6 K. **b**, Temperature dependence of the intensity of the broad main component of the EPR spectra of Cs($C_{14}H_{10}$) powder (filled brown squares). The maximum at $T_{max} \approx 42$ K coincides with that observed in $\chi(T)$ by SQUID magnetometry (open blue circles). The intensity of the weak narrow EPR component (filled green squares) follows a Curie-like dependence (solid green line) with $C = 0.0177(2)$ e.m.u. K mol^{-1} (which corresponds to ~5% of spins) and $\Theta = -2(1)$ K. After subtraction of the intensity contribution of the Curie-like line from $\chi(T)$ (open grey circles), the SQUID and EPR results coincide. Global fit of the data to a model of the $S = ½$ Heisenberg antiferromagnetic alternating chain (solid red line) yields $J/k_B = 77.9(3)$ K, $\alpha = 0.687(5)$ and $C = 0.301(1)$ e.m.u. K mol^{-1} (consistent with the $S = ½$ state of the $(C_{14}H_{10})^{\bullet-}$ radical ions). As a consistency check, we show that the total EPR spin susceptibility calculated as the sum of the antiferromagnetic chain and Curie-like contributions (dashed purple line) tracks well the measured SQUID spin susceptibility, $\chi(T)$. Inset: expanded view of the spin susceptibility at low temperatures. The solid blue line is a fit of the data up to 18 K to an exponential function, $\chi(T) \propto \exp(-\Delta/T)$ with a spin-excitation gap, $\Delta = 30.7(7)$ K.

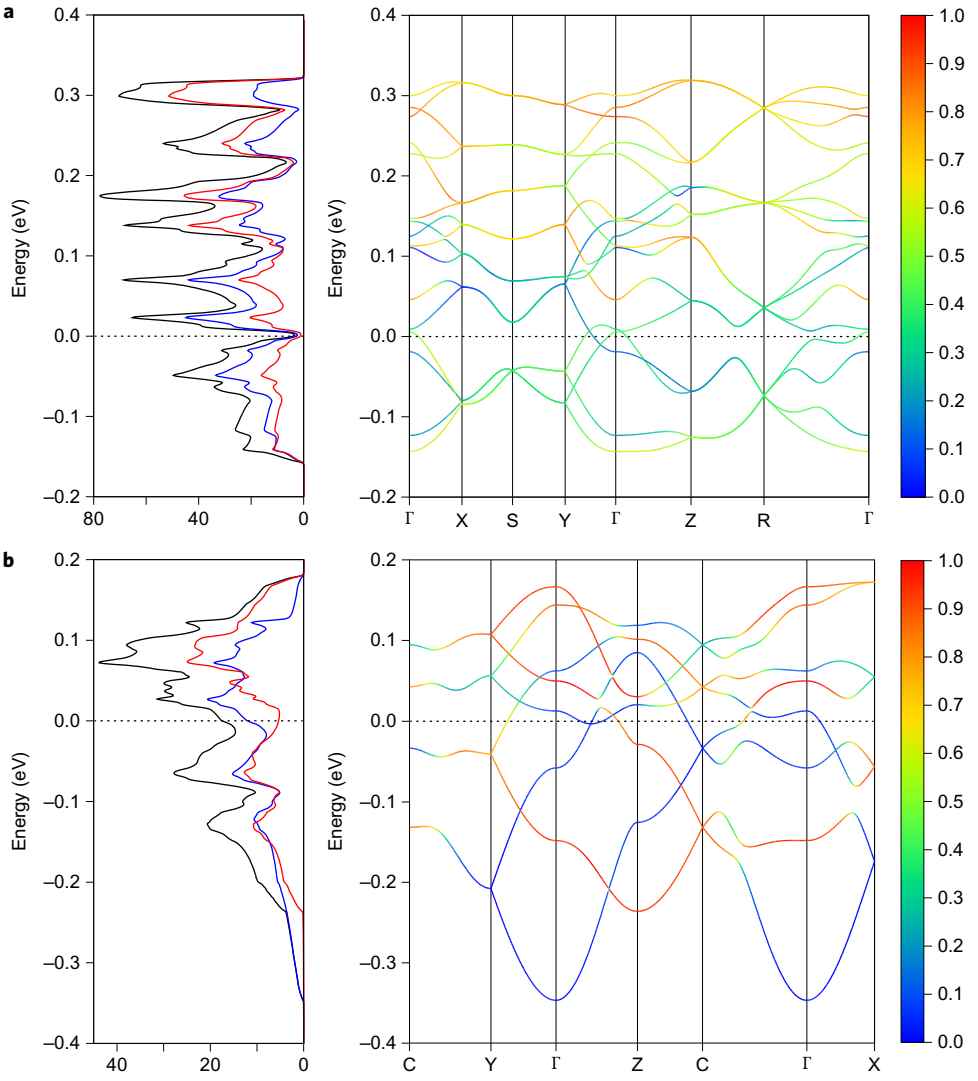

Figure 5 | Electronic band structures of $Cs(C_{14}H_{10})$ and $Cs_2(C_{14}H_{10})$. a, Calculated density of states (left) and DFT-PBE (PBE, Perdew–Burke–Ernzerhof) band dispersions (right) of $Cs(C_{14}H_{10})$. The unit cell contains eight formula units and each molecule has two nearly degenerate LUMO and LUMO+1 orbitals. Therefore, there are 16 bands in total. The energies are plotted along lines in the Brillouin zone connecting points Γ = (0,0,0), X = (½,0,0), S = (½,½,0), Y = (0,½,0), Z = (0,0,½) and R = (½,½,½). **b**, Calculated density of states (left) and DFT-PBE band dispersions (right) of $Cs_2(C_{14}H_{10})$. The unit cell contains four formula units and each molecule has two nearly degenerate LUMO and LUMO+1 orbitals. Therefore, there are eight bands in total. The energies are plotted along lines in the Brillouin zone connecting points Γ = (0,0,0), C = (0,½,½), Z = (0,0,½), Y = (0,½,0) and X = (½,0,0). The weights of the LUMO and LUMO+1 orbitals are depicted in blue and red, respectively, and the zero of the energy is at the Fermi level.

spin state and absence of AFM–LRO in **1** to temperatures as low as $T \approx 0.02J$ imply that the simplified J–αJ alternating-spin-chain model needs to be replaced by a more realistic alternative.

Strong electron correlations and magnetic frustration. First-principles electronic structure calculations of **1** and **2** within the generalized-gradient approximation (GGA) based on density functional theory (DFT) reveal that the bands originating from the LUMO and LUMO+1 orbitals are heavily entangled in both systems (Fig. 5a,b). The low-energy bands around the Fermi level are made of both molecular orbitals with energy splittings much smaller than the bandwidth ($W \approx 0.5$ eV). Therefore, on electron doping, the added electrons partially populate both bands so that $Cs(C_{14}H_{10})$ and $Cs_2(C_{14}H_{10})$ are two-orbital systems with a ¼-filled and a ½-filled band, respectively. Both systems are thus expected to be metals—this is in striking contrast with experiment, which shows that they are insulators. The absence of metallic behaviour provides the signature of the importance of strong correlations. Properly correlated first-principles calculations of the on-molecule electron-repulsion energy, U, for phenanthrene pairs in the $Cs(C_{14}H_{10})$ crystal find values that range between 1.1 and 1.8 eV (Supplementary Fig. 4 and Supplementary Table 6). As the bands in which the electrons move are narrow because of the weak intermolecular overlap, U/W is on the order of 2–3, which implies that the large on-site Coulomb repulsion could overcome the kinetic energy favouring electron delocalization (quantified by W) and lead to Mott insulating ground states for both integer, $n = 1,2$, doping levels, as observed experimentally. Hund's rule coupling, J_H, promotes insulating behaviour at half filling but diminishes the effect of correlations and leads to a reduced Mott gap in the singly occupied case[36]. However, J_H is very small in multiorbital strongly correlated molecular solids (the net Hund's coupling can be even smaller because of the presence of phonon contributions that favour a low-spin configuration)[37,38] and is therefore unable to sustain metallicity in the $n = 1$ $Cs(C_{14}H_{10})$

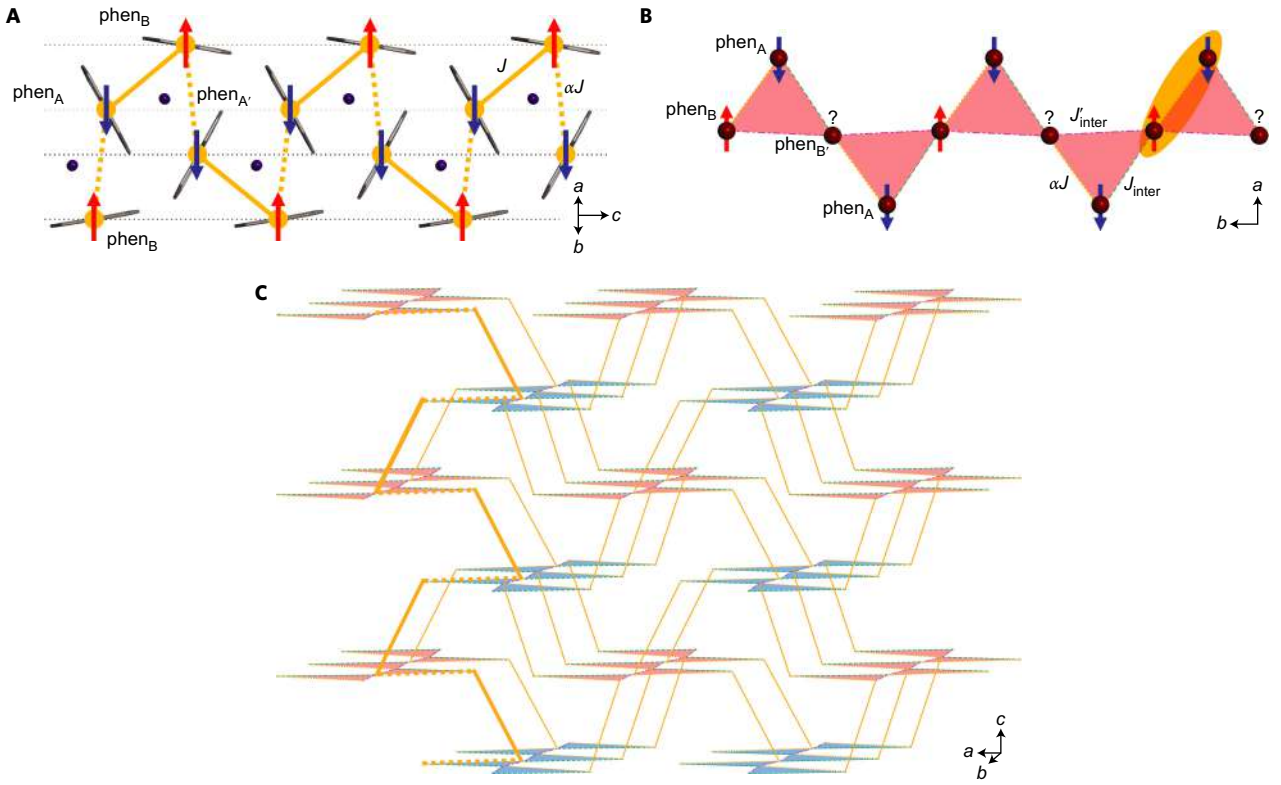

Figure 6 | First-principles calculations of the electronic and magnetic interactions in Cs($C_{14}H_{10}$). A, Alternating-exchange antiferromagnetic chain along the triangular lattice of the spin tubes aligned along the *c* axis—orange solid and dotted lines mark the strongest, *J*, and second strongest, αJ, interactions, respectively—together with a schematic representation of the non-frustrated up and down (blue and red arrows) spin topology. **B**, Diagrammatic spin configuration on the fully frustrated chains of corner-sharing triangular units (Δ chains) that link neighbouring tubes along the *b* axis. If the spin orientation of two anions is decided (blue and red arrows, with the resulting singlet shown as an orange oval), the remaining one (question mark) is left frustrated: it cannot decide with which of the two its spin should align antiparallel. The two distinct interchain couplings, J_{inter} and J'_{inter}, are depicted as green dashed and pink dot-dashed lines, respectively. **C**, Microscopic magnetic model for Cs($C_{14}H_{10}$). A staircase-like 3D interlinked arrangement arises by unequal-leg J–αJ spiral tubes running along the *c* axis that are coupled by two inequivalent couplings, J_{inter} and J'_{inter}, to form frustrated Δ chains running along the *b* axis. The same colouring scheme is used as in **A** and **B**. An example of the exchange pathway along the spin tubes is marked in thicker orange solid and dotted lines.

system. Dynamical mean-field theory (DMFT) calculations[39] of two-orbital correlated systems at half filling also reveal the existence of two fundamentally different Mott phases, a high-spin ($S = 1$) one characterized by vanishing orbital susceptibility and a low-spin ($S = 0$) one adiabatically connected to the band insulating state (that is, an orbitally polarized Mott insulating state). Materials in which J_H is very small and dominated by the level splitting[37] are found to lie in the orbitally polarized Mott insulator part of the phase diagram[39], which naturally accounts for the experimentally observed diamagnetism in $Cs_2(C_{14}H_{10})$. The effect of electron correlation in the two near-degenerate bands of $Cs_2(C_{14}H_{10})$ was confirmed explicitly by performing DFT+DMFT calculations, which establish that correlations enhance orbital polarization and push the system towards the orbitally polarized low-spin ($S = 0$) Mott state (Supplementary Fig. 5), in agreement with experiment.

The intermolecular spin interactions in **1** were evaluated by assuming an effective Heisenberg model and performing first-principles calculations on phenanthride pairs within an intermolecular centre-to-centre distance of 8.0 Å (Supplementary Table 6), considering the spin-density distribution and molecular orbital overlap. The LUMO wavefunctions—whose population on Cs is very small (Cs charge = +0.9), in agreement with the EPR experiments—are distributed over molecular pairs and exhibit biradical character, consistent with electronic localization (Supplementary Fig. 6). We found that the dominant direct antiferromagnetic interactions are between pairs of crystallographically independent $(C_{14}H_{10})_A^{\bullet-}$ and $(C_{14}H_{10})_B^{\bullet-}$ units that comprise the building components of the tubular assemblies running along the *c* axis (Fig. 1C). There are two distinct couplings with exchange constants, $J = 49$ K and $\alpha J = 44$ K, that lead to the formation of spiral magnetic tubes aligned parallel to the *c* axis and that comprise antiferromagnetically coupled alternating-exchange spin-½ molecular units (Fig. 6A). The second set of leading exchange interactions, $J_{inter} = 30$ K and $J'_{inter} = 28$ K, that emerges from the calculations corresponds to coupling between neighbouring tubes (Fig. 1D). These define a set of magnetic Δ chains—chains of corner-sharing triangular units, a fully frustrated quantum spin system[27]—running parallel to the *b* axis (Fig. 6B and Supplementary Fig. 7). The resulting 3D interlinked staircase-like spin topology is illustrated in Fig. 6C and Supplementary Fig. 8.

The salient features of the microscopic magnetic model (Fig. 6C) that emerge from the first-principles calculations can be summarized as follows: (1) the dominant exchange coupling, *J*, occurs within the *c*-axis tubes, (2) there is a small bond alternation ($\alpha \approx 0.9$), (3) interchain couplings, J_{inter} and J'_{inter} are not small ($\gamma = \langle J_{inter} \rangle / \langle J \rangle \approx 0.6$) and (4) as a result of interchain coupling, the system is highly frustrated. As *J* is the largest exchange constant, we first investigated whether the experimental $\chi(T)$ data can be reproduced by employing a model of coupled unequal-leg Heisenberg chains in which frustration in the interchain coupling has not been included. Quantum Monte Carlo (QMC) calculations were performed for three models in which a fixed sum of exchange constants was retained: (1) decoupled ($\gamma = 0$) alternating chains with

an alternation parameter $\alpha = 0.7$, (2) coupled ($\gamma = 0.3$) alternating chains with $\alpha = 0.4$ and (3) 3D uniformly coupled alternating chains with $\alpha = 0.6$ and four interchain exchange interactions in the *ab* plane with $\gamma = 0.025$. We find that the calculated uniform susceptibility (Supplementary Fig. 9) is in good agreement with experiment in all cases. However, the absence of AFM–LRO in the experiment can be reproduced by the QMC calculations only when we assume that the bond alternation is strong enough or the interchain exchange coupling is extremely small (Supplementary Fig. 9). These results necessitate that the interchain frustration, which is not considered in the present QMC calculation, is crucially important for stabilizing the spin-liquid state. The vanishing of the spin susceptibility below 6 K (~0.1 J/k_B) implies that the spins of the $(C_{14}H_{10})^{\bullet-}$ radical ions form a collective spin-singlet ground state compatible with a 3D QSL whose spin excitation spectrum has a finite gap. The magnitude of the gap opening for the spinon excitations can be extracted as $\Delta \approx 30$ K by fitting the low-temperature spin-susceptibility data to an exponential function, $\chi(T) \propto \exp(-\Delta/T)$ (Fig. 4b (inset) and Supplementary Fig. 10).

Emergence of an exotic state of matter—a 3D gapped QSL Mott insulator. The combined experimental and theoretical data described here allowed us to track the evolution of the structures and electronic states of ionic salts of phenanthrene with the change in molecular oxidation state. As the herringbone structure of pristine PAHs does not contain well-defined interstitial spaces to accommodate the alkali intercalants, intercalation is enabled only if new molecular packing motifs are adopted. Here non-herringbone-packed structures were accessed for both $Cs(C_{14}H_{10})$ and $Cs_2(C_{14}H_{10})$ compositions via solvent dissolution and reprecipitation of the phenanthrene host in the presence of reducing agents without the commonly encountered metal-bound solvent incorporation[40,41]. A complementary approach to structural engineering is offered by redox-controlled solid-state routes—these are shown to afford $K_2(C_{22}H_{14})$ salts ($C_{22}H_{14}$, picene or pentacene) with potassium intercalation enabled by cooperative molecular reorientations, which expand the herringbone packing and create new crystallographic interstices for the cations to occupy[42].

Turning to the electronic properties, both $Cs(C_{14}H_{10})$ and $Cs_2(C_{14}H_{10})$ display correlated-electron Mott localization. Although orbital degeneracy is impossible because the symmetry of the phenanthrene molecule is too low, the LUMO and LUMO+1 levels are accidentally near-degenerate and heavily entangled in the solid state—this renders **1** and **2** two-orbital systems with formal ¼- and ½-band filling in the absence of correlations (Fig. 5) and raises interesting questions as to the origin of the filling-dependent electronic behaviour. For singly occupied shells, metallicity strongly competes with the insulating state as the Mott gap is suppressed by Hund's rule coupling, J_H (ref. 36). This pertains to *d*-electron transition-metal compounds but its relevance is significantly diminished in *p*-electron molecular systems, such as $Cs(C_{14}H_{10})$, because of the small intramolecular J_H values[37,38] and so the Mott state survives. For half-filled shells, U and J_H work synergetically and the stability of the Mott state in $Cs_2(C_{14}H_{10})$ is enhanced. However, the 'low-spin' $S = 0$ state shows the dominant energy for the two electrons localized on the $(C_{14}H_{10})^{2-}$ anion by U; DFT+DMFT calculations show that the crystal-field splitting overcomes the intramolecular Hund's rule electron repulsion to stabilize one of the two quasidegenerate entangled orbitals, which is preferentially occupied by two electrons. This results in an orbitally polarized low-spin Mott insulator, which is adiabatically connected to a band-insulating state[39]. Such a state is rare among transition-metal compounds, but should be ubiquitous in correlated molecular solids at even numbers of doped carriers. Its current scarcity is presumably related to the experimental difficulty of distinguishing it from a band insulator—a label routinely used to describe diamagnetic insulating solids.

To date, QSL behaviour has been rare and its possible emergence in frustrated systems is dominated by antiferromagnetically coupled spin-½ Cu^{2+} d^9 ions adopting Kagomé magnetic topologies[4,5] and by 2D edge-sharing triangularly arranged spin-½ molecular pairs in organic charge-transfer salts close to the Mott boundary[6–8]. More-recent examples include arrangements based on d^1 ions—Kagomé networks of V^{4+} in an oxyfluoride[43] and of Cr^{5+} in $Ca_{10}Cr_7O_{28}$ with a complex frustration mechanism that involves both ferromagnetic and antiferromagnetic couplings[44]. Therefore, **1** emerges as a rare example of a spin-½ molecular quantum AFM with a frustrated 3D-interlinked exchange network based uniquely on carbon $p\pi$-electron states. Experiment here shows the absence of a transition to an ordered state even at temperatures much lower than the scale defined by the strength of magnetic interactions, J/k_B, and consistent with a large frustration parameter, $f = J/T_N$ (lower limit, $f \approx 50$). At the same time, the spin susceptibility approaches zero exponentially at low temperatures, which implies that the ground state has a zero spin and is separated from the first excited state by an energy gap. The electronic behaviour of **1** is therefore compatible with that of a 3D gapped QSL ground state as supported by the evaluated topology and strength of several different isotropic exchange couplings.

Conclusions

In summary, we have shown that by using mild conditions (this work) and by controlling the power of the reducing agents[42], it is possible both to access novel crystalline metal PAH solids with a diverse variety of molecular packing motifs and of varying molecular oxidation states, and to retain the close intermolecular contact required for a functional electronic response. Both phenanthride compounds, **1** and **2**, present examples of multiorbital strongly correlated Mott insulators, a rare phenomenon in molecular electronic materials beyond high-symmetry fullerenes[10–13]. In addition, **1** exhibits a completely new frustrated magnetic topology, and thereby emerges as an excellent candidate for realizing the long-sought $S = ½$ QSL ground state[3], here arising purely from carbon π electrons.

Methods

Synthesis of $Cs(C_{14}H_{10})$ (1) and $Cs_2(C_{14}H_{10})$ (2). Both compounds were synthesized by the reaction of Cs metal with phenanthrene in THF solution. Elemental analysis: calculated (%) for $C_{14}H_{10}Cs$, C 54.04, H 3.24; found C 54.12, H 3.28; calculated (%) for $C_{14}H_{10}Cs_2$, C 37.87, H 2.27; found C 37.36, H 2.30.

Structural analysis. Synchrotron X-ray powder diffraction data for **1** were collected between 30 and 300 K with the high-resolution multidetector diffractometer on beamline ID22 ($\lambda = 0.35420$ Å) at the European Synchrotron Radiation Facility (ESRF), Grenoble. Laboratory data for **2** were collected at ambient temperature with a Rigaku SmartLab ($\lambda = 1.54056$ Å) diffractometer operating in transmission mode. Preliminary analysis of the diffraction data was performed with the EXPO2014 suite of programs[45] using direct-space simulated-annealing approaches with the phenanthrene moieties treated as rigid bodies followed by final Rietveld refinements with the GSAS suite[46].

Vibrational spectroscopy. Infrared measurements were performed on KBr pellets with a Bruker Alpha spectrometer (resolution, 2 cm^{-1}) inside an Ar-filled glovebox. Raman spectra were collected in backscattering geometry with a Horiba Jobin Yvon LabRAM HR spectrometer with a 633 nm (at 0.37 mW power) or a 532 nm (at 0.09 mW power) laser focused to a spot of ~1 μm in diameter on samples sealed in glass capillaries. Higher laser powers led to irreversible changes.

Magnetic measurements. These were performed on samples (**1**, 31.7 mg; **2**, 31.5 mg) sealed in thin-walled quartz ampoules under a helium partial pressure (~300 mbar) with a Quantum Design SQUID MPMS magnetometer. Magnetic susceptibility, $\chi(T)$, data were collected at fields between 0.005 and 1 T (**1**) and at 5 T (**2**) under FC and at 0.005 and 0.01 T (**1**) under ZFC between 1.8 and 300 K. Magnetization, $M(H)$, measurements at ambient temperature confirmed the absence of adventitious ferromagnetic impurities in both materials. Corrections for the diamagnetic core contribution of Cs^+ and phenanthrene (-0.35×10^{-4} and -1.2086×10^{-4} e.m.u. mol^{-1}, respectively) were applied. $\chi(T)$ of **1** was fitted together

with the EPR spin susceptibility, as described below. $\chi(T)$ of **2** was fitted to the Curie–Weiss law, $\chi = \chi_0 + C/(T - \Theta)$, where χ_0 is a temperature-independent term, C is the Curie constant and Θ is the Weiss temperature.

EPR spectroscopy. X-band (~9.6 GHz) EPR experiments were performed on cooling on samples of **1** and **2** sealed under a dynamic vacuum in Suprasil quartz tubes with a homebuilt spectrometer equipped with a Varian E-101 microwave bridge and TEM104 dual-cavity resonator, and an Oxford Instruments ESR900 cryostat with an ITC503 temperature controller (stability, ±0.05 K). The microwave power was 1 mW. The EPR and SQUID $\chi(T)$ data of **1** were fitted to the expression for the magnetic susceptibility of a spin-½ antiferromagnetic alternating-exchange Heisenberg chain, described by the Hamiltonian $H = \sum_i (JS_{2i-1}S_{2i} + \alpha JS_{2i}S_{2i+1})$, where J is the intrachain exchange constant and $0 < \alpha < 1$ is an alternation parameter[32]. The SQUID data were corrected for a Curie-like defect contribution to the susceptibility by subtracting the spin susceptibility of the narrow EPR component.

DFT calculations. First-principles calculations were performed within the GGA[47] based on DFT with the QUANTUM-ESPRESSO package[48]. Ultrasoft pseudopotentials[49] and plane-wave basis sets with cutoff energies of 46 Ry for wavefunctions and 318 Ry for charge densities were used. A $3 \times 3 \times 4$ and a $4 \times 4 \times 5$ k-mesh were employed for **1** and **2**, respectively. The maximally localized Wannier functions for the low-energy bands around the Fermi level were then constructed with the Wannier90 code[50].

DFT+DMFT calculations. The effect of electron correlation on the LUMO and LUMO+1 orbitals in **2** was studied by DFT+DMFT calculations. The local (intramolecular) self-energy was calculated for each molecule in the unit cell. In practice, the calculation can be done for a single molecule by exploiting the fact that the four phenanthrene units are equivalent by symmetry. We solved the two-orbital impurity problem at a temperature of 100 K by the continuous-time quantum Monte Carlo method[51]. The intraorbital Hubbard interaction U was set to be 1 eV. The interorbital interaction U' is given by $U' = U - 2J_{\mathrm{eff}}$, where J_{eff} is the effective local exchange interaction. The double-counting correction, $\Delta\varepsilon$, at the Hartree level is subtracted from the onsite levels of LUMO and LUMO+1 orbitals; $\Delta\varepsilon$ is given by $UN_{\mathrm{LUMO}} + U'N_{\mathrm{LUMO+1}}$ and $UN_{\mathrm{LUMO+1}} + U'N_{\mathrm{LUMO}}$ for the LUMO and LUMO+1 orbitals, respectively (N, orbital occupation at the DFT level). The small orbital off-diagonal self-energy was neglected in the DMFT simulation.

Quantum-chemical calculations. Spin-flip and on-site electron repulsion U energies were calculated by properly correlated first-principles calculations using multireference second-order perturbation theory (MRMP2) with CASSCF (complete active-space self-consistent field)-optimized orbitals in which the active space consists of singly occupied LUMOs of two molecules (the MRMP2(2,2) method) (Supplementary Fig. 6). We employed the double-zeta valence basis set with the SBKJC pseudopotential, in which (p,d) polarization and (s,p) diffuse functions are added for the phenanthrene units.

QMC calculations. The magnetic susceptibility was evaluated by applying the loop cluster algorithm implemented in the code LOOP in the ALPS libraries[52] on 16,000 sites ($20 \times 20 \times 40$). Statistical errors were confirmed to be low enough in the plot by using 5,000 thermalization steps and 10,000 sweeps after thermalization.

Data availability. All data are included in the main text and Supplementary Information and/or are available from the corresponding authors on request.

Received 15 September 2016; accepted 6 March 2017; published online 24 April 2017

References

1. Ramirez, A. P. Strongly geometrically frustrated magnets. *Annu. Rev. Mater. Sci.* **24,** 453–480 (1994).
2. Balents, L. Spin liquids in frustrated magnets. *Nature* **464,** 199–208 (2010).
3. Imai, T. & Lee, Y. S. Do quantum spin liquids exist? *Phys. Today* **69,** 30–36 (2016).
4. Fu, M., Imai, T., Han, T.-H. & Lee, Y. S. Evidence for a gapped spin-liquid ground state in a Kagomé Heisenberg antiferromagnet. *Science* **350,** 655–658 (2015).
5. Okamoto, Y., Yoshida, H. & Hiroi, Z. Vesignieite $BaCu_3V_2O_8(OH)_2$ as a candidate spin-½ Kagomé antiferromagnet. *J. Phys. Soc. Jpn* **78,** 033701 (2009).
6. Shimizu, Y., Miyagawa, K., Kanoda, K., Maesato, M. & Saito, G. Spin liquid state in an organic Mott insulator with a triangular lattice. *Phys. Rev. Lett.* **91,** 107001 (2003).
7. Itou, T., Oyamada, A., Maegawa, S., Tamura, M. & Kato, R. Spin-liquid state in an organic spin-½ system on a triangular lattice, $EtMe_3Sb[Pd(dmit)_2]_2$. *J. Phys. Condens. Matter* **19,** 145247 (2007).
8. Isono, T. *et al.* Gapless quantum spin liquid in an organic spin-½ triangular-lattice κ–H_3(Cat-EDT-TTF)$_2$. *Phys. Rev. Lett.* **112,** 177201 (2014).
9. Saito, G. & Yoshida, Y. Development of conductive organic molecular assemblies: organic metals, superconductors, and exotic functional materials. *Bull. Chem. Soc. Jpn* **80,** 1–137 (2007).
10. Takabayashi, Y. *et al.* The disorder-free non-BCS superconductor Cs_3C_{60} emerges from an antiferromagnetic insulator parent state. *Science* **323,** 1585–1590 (2009).
11. Ganin, A. Y. *et al.* Polymorphism control of superconductivity and magnetism in Cs_3C_{60} close to the Mott transition. *Nature* **466,** 221–225 (2010).
12. Zadik, R. H. *et al.* Optimized unconventional superconductivity in a molecular Jahn–Teller metal. *Sci. Adv.* **1,** e1500059 (2015).
13. Ganin, A. Y. *et al.* Bulk superconductivity at 38 K in a molecular system. *Nat. Mater.* **7,** 367–371 (2008).
14. Veciana, J. *π-Electron Magnetism. From Molecules to Magnetic Materials* (Springer, 2001).
15. Yamaguchi, H. *et al.* Unconventional magnetic and thermodynamic properties of $S = ½$ spin ladder with ferromagnetic legs. *Phys. Rev. Lett.* **110,** 157205 (2013).
16. Riyadi, S. *et al.* Antiferromagnetic $S = ½$ spin chain driven by p-orbital ordering in CsO_2. *Phys. Rev. Lett.* **108,** 217206 (2012).
17. Klanjšek, M. *et al.* Phonon-modulated magnetic interactions and spin Tomonaga–Luttinger liquid in the p-orbital antiferromagnet CsO_2. *Phys. Rev. Lett.* **115,** 057205 (2015).
18. Mitsuhashi, R. *et al.* Superconductivity in alkali-metal-doped picene. *Nature* **464,** 76–79 (2010).
19. Wang, X. F. *et al.* Superconductivity at 5 K in alkali-metal-doped phenanthrene. *Nat. Commun.* **2,** 507 (2011).
20. Xue, M. *et al.* Superconductivity above 30 K in alkali-metal-doped hydrocarbon. *Sci. Rep.* **2,** 389 (2012).
21. Kosugi, T. *et al.* First-principles electronic structure of solid picene. *J. Phys. Soc. Jpn* **78,** 113704 (2009).
22. de Andres, P. L., Guijarro, A. & Vergés, J. A. *Ab initio* electronic and geometrical structures of tripotassium-intercalated phenanthrene. *Phys. Rev. B* **84,** 144501 (2011).
23. Mahns, B., Roth, F. & Knupfer, M. Absence of photoemission from the Fermi level in potassium intercalated picene and coronene films: structure, polaron, or correlation physics? *J. Chem. Phys.* **136,** 134503 (2012).
24. Ruff, A. *et al.* Absence of metallicity in K-doped picene: importance of electronic correlations. *Phys. Rev. Lett.* **110,** 216403 (2013).
25. Naghavi, S. S. & Tosatti, E. Crystal structure search and electronic properties of alkali-doped phenanthrene and picene. *Phys. Rev. B* **90,** 075143 (2014).
26. Heguri, S., Kobayashi, M. & Tanigaki, K. Questioning the existence of superconducting potassium doped phases for aromatic hydrocarbons. *Phys. Rev. B* **92,** 014502 (2015).
27. Kubo, K. Excited states and the thermodynamics of a fully frustrated quantum spin chain. *Phys. Rev. B* **48,** 10552–10555 (1993).
28. Kay, M. I., Okaya, Y. & Cox, D. E. A refinement of the structure of the room temperature phase of phenanthrene, $C_{14}H_{10}$, from X-ray and neutron diffraction data. *Acta Cryst. B* **27,** 26–33 (1971).
29. Kato, T., Yoshizawa, K. & Hirao, K. Electron–phonon coupling in negatively charged acene- and phenanthrene-edge-type hydrocarbon crystals. *J. Chem. Phys.* **116,** 3420–3429 (2002).
30. Kuzmany, H., Matus, M., Burger, B. & Winter, J. Raman scattering in C_{60} fullerenes and fullerides. *Adv. Mater.* **6,** 731–745 (1994).
31. Kosaka, M. *et al.* Superconductivity in Li_xCsC_{60} fullerides. *Phys. Rev. B* **59,** R6628–R6630 (1999).
32. Johnston, D. C. *et al.* Thermodynamics of spin $S = ½$ antiferromagnetic uniform and alternating-exchange Heisenberg chains. *Phys. Rev. B* **61,** 9558–9606 (2000).
33. Oshikawa, M. & Affleck, I. Low-temperature electron spin resonance theory for half-integer spin antiferromagnetic chains. *Phys. Rev. Lett.* **82,** 5136–5139 (1999).
34. Furuya, S. C. & Sato, M. Electron spin resonance in quasi-one-dimensional quantum antiferro-magnets: relevance of weak interchain interactions. *J. Phys. Soc. Jpn* **84,** 033704 (2015).
35. Lemmens, P., Güntherodt, G. & Gros, C. Magnetic light scattering in low-dimensional quantum spin systems. *Phys. Rep.* **375,** 1–103 (2003).
36. de' Medici, L., Mravlje, J. & Georges, A. Janus-faced influence of Hund's rule coupling in strongly correlated materials. *Phys. Rev. Lett.* **107,** 256401 (2011).
37. Nomura, Y., Nakamura, K. & Arita, R. *Ab initio* derivation of electronic low-energy models for C_{60} and aromatic compounds. *Phys. Rev. B* **85,** 155452 (2012).
38. Nomura, Y. *et al.* Unified understanding of superconductivity and Mott transition in alkali-doped fullerides from first principles. *Sci. Adv.* **1,** e1500568 (2015).
39. Werner, P. & Millis, A. J. High-spin to low-spin and orbital polarization transitions in multiorbital Mott systems. *Phys. Rev. Lett.* **99,** 126405 (2007).
40. Smith, J. D. Organometallic compounds of the heavier alkali metals. *Adv. Organomet. Chem.* **43,** 267–348 (1999).
41. Zabula, A. V. & Petrukhina, M. A. Structural perspective on aggregation of alkali metal ions with charged planar and curved carbon π-surfaces. *Adv. Organomet. Chem.* **61,** 375–462 (2013).
42. Romero, F. D. *et al.* Redox-controlled potassium intercalation into two polyaromatic hydrocarbon solids. *Nat. Chem.* http://dx.doi.org/10.1038/nchem.2765 (2017).
43. Aidoudi, F. H. *et al.* An ionothermally prepared $S = ½$ vanadium oxyfluoride Kagomé lattice. *Nat. Chem.* **3,** 801–806 (2011).

44. Balz, C. *et al.* Physical realization of a quantum spin liquid based on a complex frustration mechanism. *Nat. Phys.* **12,** 942–949 (2016).
45. Altomare, A. *et al. EXPO2013*: a kit of tools for phasing crystal structures from powder data. *J. Appl. Crystallogr.* **46,** 1231–1235 (2013).
46. Larson, A. C. & von Dreele, R. B. *General Structure Analysis System (GSAS)* (Los Alamos National Laboratory Report No. LAUR 86-748, 2000).
47. Perdew, J. P., Burke, K. & Ernzerhof, M. Generalized gradient approximation made simple. *Phys. Rev. Lett.* **77,** 3865–3868 (1996).
48. Giannozzi, P. *et al.* QUANTUM ESPRESSO: a modular and open-source software project for quantum simulations of materials. *J. Phys. Condens. Matter* **21,** 395502 (2009).
49. Vanderbilt, D. Soft self-consistent pseudopotentials in a generalized eigenvalue formalism. *Phys. Rev. B* **41,** 7892(R)–7895(R) (1990).
50. Mostofi, A. A. *et al.* Wannier90: a tool for obtaining maximally-localised Wannier functions. *Comput. Phys. Commun.* **178,** 685–699 (2008).
51. Nomura, Y., Sakai, S. & Arita, R. Multiorbital cluster dynamical mean-field theory with an improved continuous-time quantum Monte Carlo algorithm. *Phys. Rev. B* **89,** 195146 (2014).
52. Bauer, B. *et al.* The ALPS project release 2.0: open source software for strongly correlated systems. *J. Stat. Mech. Theor. Exp.* P05001 (2011).

Acknowledgements

This work was sponsored by the World Premier International (WPI) Research Center Initiative for Atoms, Molecules and Materials, Ministry of Education, Culture, Sports, Science and Technology of Japan. We acknowledge financial support from the Japan Science and Technology Agency under the ERATO Isobe Degenerate π-Integration Project, the Mitsubishi Foundation, the Japan Society for the Promotion of Science (JSPS) under the Scientific Research on Innovative Areas 'J-Physics' Project (No. 15H05882), the European Union/JST SICORP-LEMSUPER FP7-NMP-2011-EU-Japan project (contract no. NMP3-SL-2011-283214), the UK Engineering and Physical Sciences Research Council (grant nos EP/K027255 and EP/K027212) and the Slovenian Research Agency (grant no. N1-0052). We thank the ESRF for access to synchrotron X-ray facilities, the Royal Society for a Newton International Fellowship (G.K.) and a Research Professorship (M.J.R.), A. N. Fitch for help with the synchrotron XRD experiments, H. Okazaki with the magnetic measurements and K. Kamarás with the infrared measurements.

Author contributions

K.P. and M.J.R. conceived and designed the project. K.P. directed and coordinated the research. Y.T. and M.M. interpreted and discussed all the results and carried out the final structural and magnetic work. H.T., N.T., T.K., Y.N. and R.A. carried out the calculations. A.Š. synthesized the materials. D.A. carried out the EPR spectroscopy and G.K. the vibrational spectroscopic work. A.J.C.B. and A.Š. carried out early structural and magnetic work. K.P. wrote the paper with input from all the authors.

Additional information

Supplementary information is available in the online version of the paper. Reprints and permissions information is available online at www.nature.com/reprints. Publisher's note: Springer Nature remains neutral with regard to jurisdictional claims in published maps and institutional affiliations. Correspondence and requests for materials should be addressed to M.J.R. and K.P.

Competing financial interests

The authors declare no competing financial interests.